K. Günaydın, Z. Eren, Z. Kazancı, F. Scarpa, A.M. Grande, H.S. Türkmen
In-Plane Compression Behavior of Anti-Tetrachiral and Re-Entrant Lattices
Smart Materials and Structures, Vol. 28, 2019, 115028 (14 pages)
doi:10.1088/1361-665X/ab47c9

in-plane compression behavior of anti-tetrachiral and re-entrant lattices

IN-PLANE COMPRESSION BEHAVIOR OF ANTI-TETRACHIRAL AND RE-ENTRANT LATTICES

Kadir Günaydın [a, b*]

Zana Eren [a, c]

Zafer Kazancı [d]

Fabrizio Scarpa [e]

Antonio Mattia Grande [b]

Halit Süleyman Türkmen [a]

[a] Faculty of Aeronautics and Astronautics, Istanbul Technical University, 34469, Maslak, Istanbul, Turkey

[b] Department of Aerospace Science and Technology, Politecnico di Milano, Via La Masa 34, 20156 Milano, Italy

[c] Laboratory for Multiscale Mechanics (LM2), Department of Mechanical Engineering, Ecole Polytechnique de Montréal, C.P. 6079, Montreal, Quebec H3C 3A7, Canada

[d] School of Mechanical & Aerospace Engineering, Queen's University Belfast, Belfast, United Kingdom

[e] Bristol Composites Institute (ACCIS), University of Bristol, BS8 1TR, Bristol, United Kingdom

*kadir.gunaydin@polimi.it; erenza@itu.edu.tr; z.kazanci@qub.ac.uk; f.scarpa@bristol.ac.uk; antoniomattia.grande@polimi.it; halit@itu.edu.tr

ABSTRACT

In the present study, a comparative compression investigation of anti-tetrachiral and modified re-entrant lattices was conducted in-plane direction using experimental and numerical analyses. Lattice structures were manufactured using fused deposition modelling (FDM) 3D printing technology and crushed at quasi-static condition. Non-linear finite element (FE) models of both structures were established, and the FE results were systematically compared with the experimental results. The onset of densification phases of both structures was determined numerically. Results indicate that deformation modes strongly affect the force-deflection response of both designs. In this manner, failure locations and buckling deformation in the tests were identified to find a relation with theory and to modify geometries. The anti-tetrachiral design exhibits higher specific energy absorption than modified re-entrant hexagonal lattices. Beyond the auxetic characteristics, deformation mechanism of the anti-tetrachiral lattices provides an opportunity to construct excellent crush absorption in-plane direction thanks to its high shear strength stem from its unique deformation mechanism.

Keywords:

1. Anti-tetrachiral
2. Re-entrant
3. Auxetic
4. Crushing
5. Numerical analysis
6. 3D printing

1. INTRODUCTION

In aerospace, automotive, marine, and military applications, low-density lightweight structures such as sandwich structures have an important role considering crush resistance during impact and blast situations. For crashworthy structures, different types of lightweight sandwich structures have been proposed with different cores such as foams, lattices, and trusses because they offer very small weight to area ratio while retaining excellent rigidity, strength, and impact energy absorption abilities [1]. The lattice cores have come forward regarding crashworthiness, and one of the most promising lattice structures are auxetic cellular solid structures [2]. Auxetic cellular solid structures are a special type of structures exhibiting negative Poisson's ratio (NPR) with anti-rubber or dilatational features by experiencing lateral expansion under tensile loads and shrinkage with the effect of compressive loads. In addition to large global flexibility and large local deformation within elastic limits, the enhanced mechanical properties of auxetic materials, can be listed compared to traditional materials as follows: (a) improved edgewise (in-plane) indentation resistance (b) high fracture toughness (c) better transverse shear modulus [3]. Due to their superior properties, auxetic structures have been utilized in various applications such as innovative stent designs [4,5], smart actuators, propellers, flexible microelectronics, and biomechanical devices [6,7]. Additionally, special auxetic structures are tailored for the coefficient of thermal expansions [8]. There are several studies in the literature about NPR structures, however, the first artificial synthetic foam material having negative Poisson's ratio was introduced by Lake [9] in 1987, and the terminology of auxetic was first proposed by Evans in 1991 [2]. Structures with NPR are also termed as metamaterials because of their unique properties beyond conventional ones [10–15]. These unique properties are obtained through geometrical configurations. Adjusting Young's modulus or Poisson's ratio can be succeeded through modifying geometrical parameters of the unit cell, which are the repeated smallest topology of the network. Classification of different types of auxetic structures can be found in the literature [16–18].

Auxetic structures can be offered as crashworthy structures regarding their energy absorption characteristics that can be tuned by the change of geometrical parameters. In particular, it is known that the energy absorption capability of the cellular materials is closely related to relative density, the thickness of the cell walls and the angle

between walls [19,20]. Generally, hexagonal honeycomb structures are used as a core structure for sandwich structures. Nakamoto et al. [21] presented an analytical approach for the progressive and plastic in-plane collapse of hexagonal lattices. Re-entrant structures can be obtained as a result of hexagonal structures modification by changing the interior angles of adjacent cell walls greater than 180^{o}. Zhou et al. [22] investigated the plastic in-plane compression behavior of re-entrant lattices. Several researchers introduced the elasticity equations of different lattices exhibiting NPR [13,23–27] and zero Poisson's ratio (ZPR) [28]. For instance, Chen et al. [29] calculated the in-plane elasticity equations of anti-tetrachiral lattices and compared with the experimental results. Innovative novel 2D designs of tetrachiral and anti-tetrachiral auxetic lattices were proposed by Huimini et al. [1] and Wengwang [30]. In their studies, analytical expressions are derived for the in-plane mechanical properties and validated with FEA and experimental results. A large deformation compression studies were conducted for anti-trichiral honeycomb specimens with various ligament length which are produced by ABS polymer by cutting with a laser. As a result of studies, the ratio of ligament length to node radius is to be less than 5.5 for the exhibition of auxeticity, and the increase of the ratio of the oblique ligament to horizontal ligament increases the global stress and specific energy [31,32]. In addition, a study was conducted for the 3D isotropic anti-tetrachiral structure. An expression based on rigid cubic node rotation and kinematic deformation geometrical relation was constituted in the study by validating experimental and FEA results to obtain dimensionless geometrical parameters for tuning [33]. Moreover, 3D novel designs called chiral- chiral- antichiral and chiral- antichiral– antichiral auxetic lattices were proposed and their compression performances were compared [34]. Huang et al. [26] have studied the in-plane elasticity equation of modified re-entrant hexagonal lattices. They have modified re-entrant cells to make the structure stronger against the possible out-of-plane loading. Chen and Fu [35] modified 3D re-entrant lattices and obtained better stiffness comparing typical re-entrant design. However, there are a few experimental and numerical studies on the elastic and plastic collapse behavior of auxetic lattice structures. Zhang et al. [36] conducted a parametric study for the dynamic crushing response of re-entrant honeycombs with different cell angles at different strain rates. Ingrole et al. [37] manufactured 3D auxetic lattices with re-entrant unite cells and investigated their in-plane static crushing response suggesting modified re-entrant cells for better energy absorption. Zhou et al. [22] have investigated plastic

collapse behavior of metal re-entrant lattice structure by changing some geometrical parameters. Ren et al. [38] proposed a buckling induced auxetic design composed of a solid sphere and three cuboids. However, this study only deals with the elastic behavior of the auxetic design. Additionally, some re-entrant lattice compression studies were performed under quasi-static and dynamic loads. Dong et al. [39] investigated the effect of cell-wall thickness on the deformation mode indicating that thickness greater than 0.4 mm shows deformation mode similar to thick-walled honeycombs. A numerical and experimental study [40] on the uni- and bidirectionally graded re-entrant auxetic honeycomb's compression behavior to investigate the deformation mode and Poisson's ratio distribution, and a numerical dynamic compression research [41] on regular re-entrant auxetic honeycomb under the low, medium, and high-velocity compressions for the investigation of the effect of inertia on NPR were performed.

In this research, quasi-static crushing response of anti-tetrachiral [13] and modified re-entrant hexagonal [26] lattices which exhibit in-plane negative Poisson's ratio were investigated. Re-entrant lattices have been used as comparing geometry against anti-tetachiral lattices. This work is devoted to giving an insight into the in-plane compressive response of these 3D printed lattices in the plastic region. For this purpose, lattice structures have been manufactured via fused deposition modelling (FDM) technique and tested in quasi-static condition. Later, models were simulated by Finite Element Analysis (FEA) using commercial software, ABAQUS. The deformation mechanism of lattice structures was observed and modelled in order to understand the relationship between failure, deformation modes, and force response.

2. LATTICE GEOMETRIES

Anti-tetrachiral and modified re-entrant lattices exhibiting NPR in-plane direction and in the elastic phase were crushed at the quasi-static condition to observe their elastic and plastic deformation. First of all, formulation on the strength of structures in the y-direction, where auxeticity is experienced, and its relation with other parameters were given in this section.

The chiral auxetic system can be defined by the interconnected systems of nodes and ligaments, each tip of the ligaments is connected to the nodes tangentially. The

number of the ligaments connected to one node characterises the chiral honeycombs as hexachiral, tetrachiral and trichiral systems which include 6, 4 and 3 tangential ligaments for each node, respectively. The prefix anti is used to describe the spatial relations between ligaments and nodes; lattice structures with cylindrical nodes on the opposite sides of the ligaments are called chiral systems, and conversely, cylinders on the same side of the ligament are called antichiral systems. However, all the chiral systems do not show auxeticity, 6 and 4 ligaments connected systems and the anti-trichiral systems with short ligament limit only show negative Poisson's ratio [25]. The deformation of chiral systems starts with the rotation of nodes, and flexing and bending of the ligaments as a result of rotation. Then ligaments become half wave-shaped for antichiral systems and full wave-shaped, which is better for energy absorption, for chiral systems [10]. Although anti-tetrachiral and re-entrant auxetic systems have similar outline topology, the deformation mechanisms are quite different. Based on the unit cell deformation mechanism, re-entrant structures have the diagonal ligaments leads to auxetic effect by ligament rotations, and chiral structures maintain auxeticity by the coupled deformation of node rotation and ligament bending. Basic re-entrant auxetic structure and honeycomb structure have been studied for many years, and comparison studies according to energy absorption for both topologies can be found in the literature. As a result of comparisons, re-entrant auxetic structures show low initial peak force and better mean crushing load to initial peak load ratio beside better energy absorption [35, 43].

2.1. Anti-tetrachiral

The anti-tetrachiral lattice is composed of four edge ligaments, and a possible compressive deformation develops through bending moments around these ligaments. Chen et al. [29] presented elasticity equations for anti-tetrachiral lattices parameters that are presented in Figure 1. The results provide a better understanding of the relation between modulus parameters (E_x, E_y andG_{xy}), geometrical parameters ($\alpha_x(=\frac{L_x}{r})$, α_y $(=\frac{L_y}{r})$), and Poisson's ratio. By this means, these elastic relations benefit to design stiffer unit lattice. Young's modulus of anti-tetrachiral lattice honeycombs was defined as in Equations (1) and (2) [29] as follows:

$$E_x = \frac{E_c \beta^3 \alpha_x}{12\left(1-\frac{\beta}{2}\right)^2 \alpha_y}\left(\frac{1}{\alpha_x - 2\sqrt{2\beta-\beta^2}} + \frac{1}{\alpha_y - 2\sqrt{2\beta-\beta^2}}\right) \quad (1)$$

$$E_y = \frac{E_c \beta^3 \alpha_y}{12\left(1-\frac{\beta}{2}\right)^2 \alpha_x}\left(\frac{1}{\alpha_x - 2\sqrt{2\beta-\beta^2}} + \frac{1}{\alpha_y - 2\sqrt{2\beta-\beta^2}}\right), \quad (2)$$

where α_x, α_y and β equals to L_x/r, L_y/r and t/r respectively.

Dimensions of the manufactured sample were listed in Table 1. These dimensions have been selected due to the manufacturing constraints of the ZOTRAX 3D printer. Smaller L_x, L_y parameters were selected due to global buckling risk under static crushing conditions. When Equation 2 is revisited, it is concluded that scaling the unit lattices down to half of it, α_x, α_y and β stay the same as before, and relative volume increases the same as relative density.

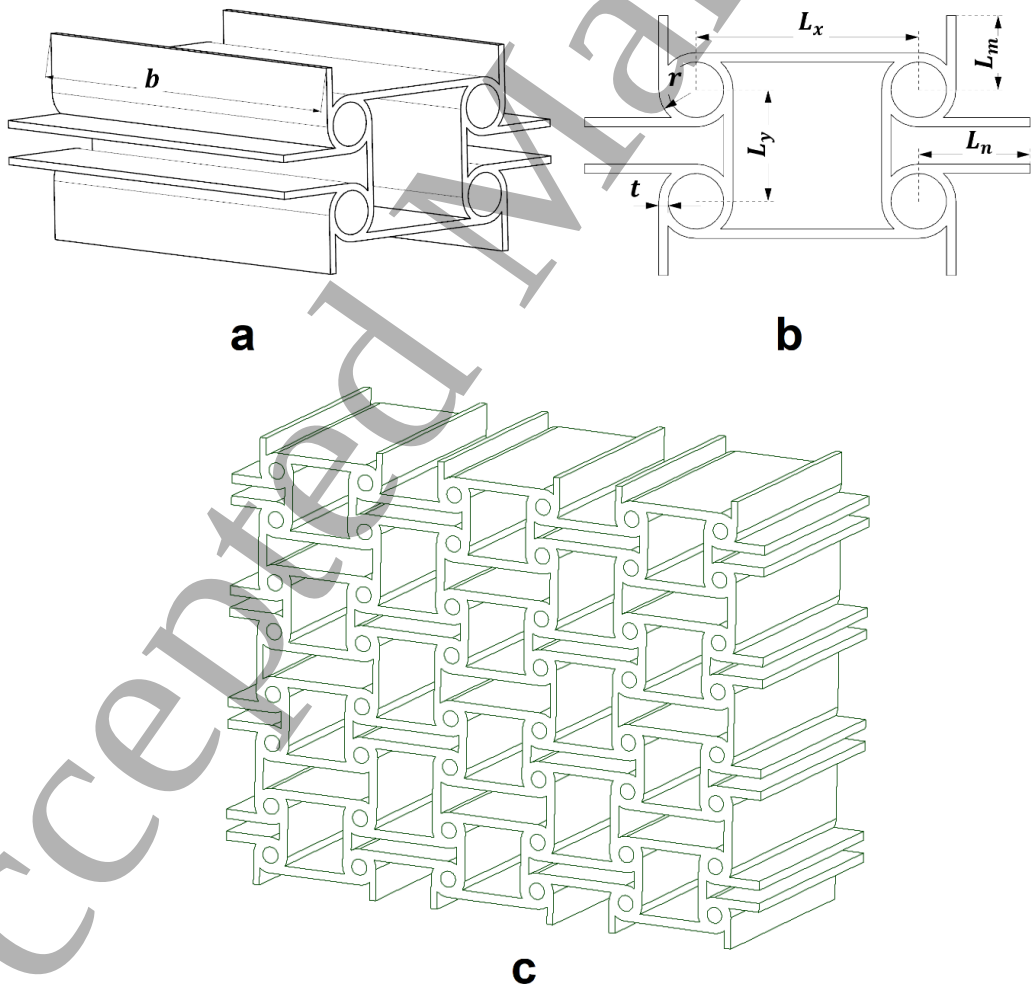

Figure 1. Anti-tetrachiral unit cell a) iso-view b) front-view c) manufactured sample.

Table 1. Geometrical parameters of the manufactured anti-tetrachiral samples.

	L_x	L_y	r	t	b	L_m	L_n
Planned	12 mm	6 mm	2 mm	1 mm	28 mm	4 mm	6 mm
Manufactured	12 mm	6.55 mm	2.4 mm	1.25 (±0.25) mm	28 mm	4.5 mm	6.5 mm

In addition to E_x and E_y formulations, when the relative density of honeycomb structure has been increased, lattice system becomes stiffer in the z-direction (out of plane) since these cellular topologies are thought to have a uniform wall thickness and depth [20]. The relation between E_z and E_c, the elastic modulus of constituent material, are defined by the density of the lattice system which is given in Equation 3:

$$\frac{E_z}{E_c} = \frac{\rho}{\rho_c} \tag{3}$$

in which ρ_c and ρ denote core material and lattice structure densities, respectively. Another representation with a relation between core material area (A_c) and unit cell area (A_u) relevant to the density of the cell-based core structures is obtained as:

$$\frac{\rho}{\rho_c} = \frac{A_c}{A_u} = \frac{A_n + A_l - A_j}{A_u} \tag{4}$$

where A_n, A_l and A_j are nodes, ligaments and junction areas of each unit lattice [42].

The increased surface area does not change E_x and E_y if α_x, α_y and β are constant [29]. Therefore, scaling down of a unit lattice system with constant α_x and α_y do not change E_x and E_y, but increases relative density. While the relation between energy absorption and relative density at dynamic crushing regimes depends on the unit cell geometry, in the quasi-static regime, increased relative density benefits the energy absorption [43,44]. According to the formulations in Equation 1 and Equation 2, geometries can be tuned to obtain higher E_x and E_y values. However, E_y increases when α_y is increased and α_x is decreased or E_x increases when α_x is increased and α_y is decreased. Due to this inverse relationship, higher E_y is required for higher

stiffness in the y-direction loading. Consequently, L_m and L_n are selected as equal to 2, and α_x and α_y are defined as 3 and 6, respectively to obtain higher E_y.

2.2. Re-entrant Hexagonal

As another example of auxetic lattice geometries, Huang et al. [45] proposed the modified re-entrant hexagonal geometry for in-plane auxetic behavior and high bending stiffness in the out of the plane. Unit cell parameters and dimensions have been presented in Figure 2 and Table 1.

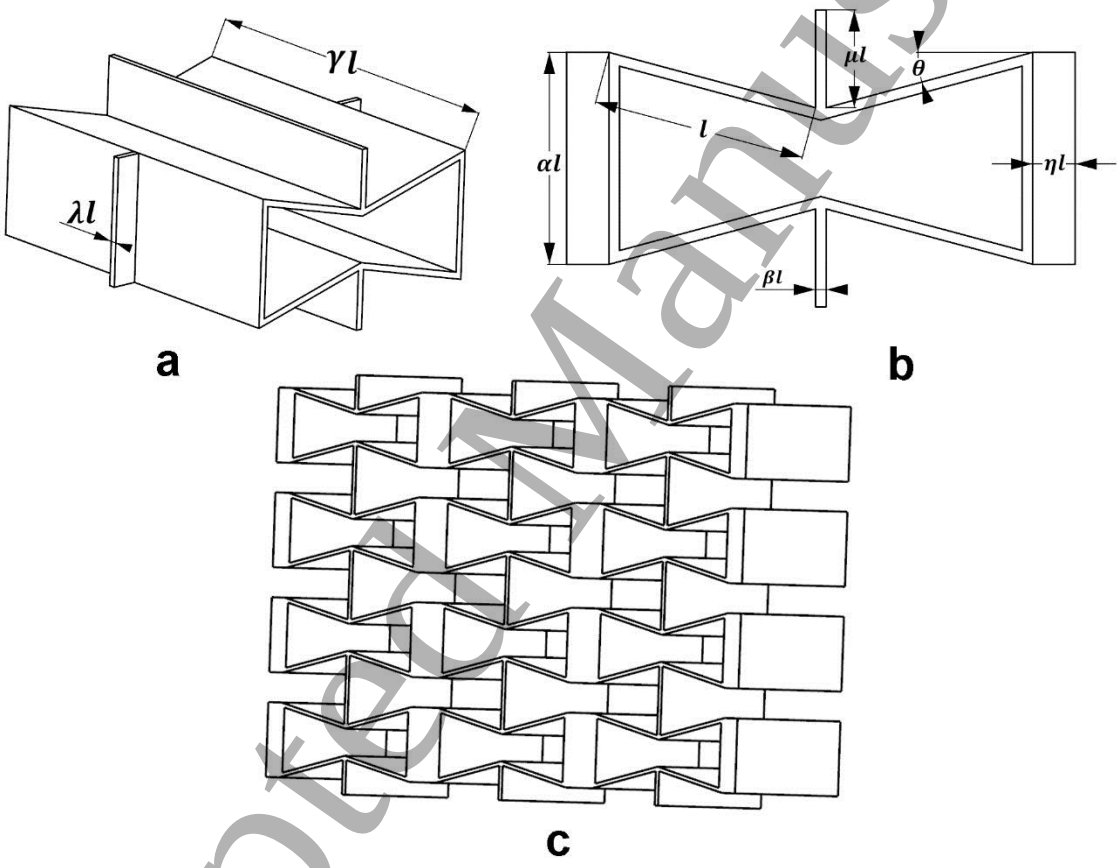

Figure 2. Re-entrant hexagonal unit cell a) iso-view b) front-view c) manufactured sample.

Table 2. Geometrical parameters of the manufactured modified re-entrant samples.

l	α	β	μ	λ	γ	η	θ	ϑ_{xy}
10 mm	1	0.1	0.46 (-0.04)	2.8	2.8 (+0.05)	0.1	15°	-0.6

However, the modified re-entrant hexagonal geometry proposed by Huang et al. [45] was used for in-plane compression tests. It was observed that the connections between each unit cells were broken down prematurely. The results regarding thin joint walls were presented in our previous work [46]. Therefore, the sidewalls of the modified re-entrant lattices were thickened with the equality of the $\lambda l = \gamma l$. This geometry was taken into account to compare with anti-tetrachiral lattices. It was reported that the modified re-entrant lattices exhibited high out-of-plane strength [45]. Moreover, the compressive deformation was investigated in the in-plane direction where auxetic behavior is present. Both the limit of auxeticity and subsequent plastic buckling phase can be observed. The elastic moduli in two directions were defined in Equation 5 and Equation 6 as:

$$\frac{E_x}{E_S} = \frac{\alpha\lambda\beta^3\left(\eta + \cos\theta + \frac{\beta}{2}\right)}{\frac{1}{2}\alpha + \mu - \sin\theta\left[\alpha\lambda(\sin^2\theta + \beta^2\cos^2\theta) + 2\eta\gamma\beta^3\right]} \tag{5}$$

$$\frac{E_y}{E_S} = \frac{\beta^3\left(\frac{\alpha}{2} + \mu - \sin\theta\right)}{\left(\eta + \cos\theta + \frac{\beta}{2}\right)(2\mu\beta^2 + \beta^2 + \cos^2\theta - \beta^2\cos^2\theta)} \tag{6}$$

where α, β, η, λ, μ, and γ denotes geometrical non-dimensional parameters of the re-entrant hexagonal lattice depicted in Figure 2. The internal cell angle is represented by θ. The length of the inclined walls is represented by l. It is shown that wall thickness and top-bottom struts affect the stiffness. However, compression response is sensitive to global buckling (slenderness) and local bucklings that are the results of non-dimensional parameters.

3. EXPERIMENTAL SETUP

Two different auxetic geometries were manufactured using FDM technique on Zortrax M200 3D printer with acrylonitrile butadiene styrene (ABS) polymer build material. Elastic material properties of the ABS are provided by the supplier; Young's modulus, Poisson's ratio, and density were given as 1850 MPa, 0.35 and 1040 kg/m^3, respectively [47]. However, provided material specifications are different from the

manufactured ones due to FDM manufacturing method characteristics. In FDM, a nozzle deposits melted polymer layer by layer, and the formation of inner gaps cannot be prevented. Besides, different infill patterns and strategies are employed in FDM for thick parts to prevent the wrapping of manufactured parts. Thus, thinner tensile specimens can be selected to reduce the magnitude of inner gaps and to obtain solid infill approaching constituent material specifications. EN ISO 527-3 standard was used to obtain tensile test results. All the tensile specimens were printed at 90º raster orientation which is parallel to building plate, and test set-up is shown in Figure 3. Tensile tests were carried out using an INSTRON 5980 100 kN Universal Testing System with AVE 2 non-contacting video extensometer and its own commercial DIC software. Tensile results are illustrated in Figure 4 and measured mechanical and physical material properties were listed in Table 3.

The 3D printer resolution for the production was selected as 0.09 mm for both geometries, and infill was chosen as maximum to avoid empty spaces. Manufactured samples were illustrated in Figure 5. The quasi-static in-plane crushing tests were conducted using INSTRON 5980 100 kN Universal Testing System with a crushing speed of 10 mm/min. Load change and the displacement of the crosshead values were recorded.

The wall thickness dimensions for lattice structures were selected as 1 mm to manufacture solid infilled lattice structures. All test sample dimensions were listed in Table 1 and Table 2. Both designs were manufactured to obtain a similar box-volume (Figure 5).

Figure 3. Tensile test setup using the method of advanced video extensometer.

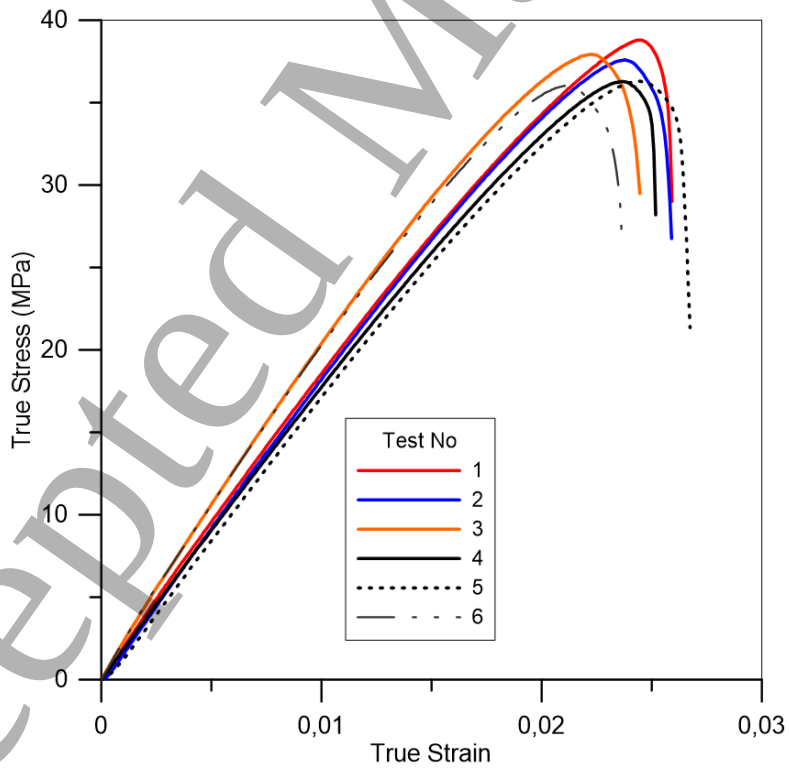

Figure 4. Tensile test results of the ABS material.

Table 3. Material properties of the 3D printing specimens

Young's Modulus (GPa)	Tensile strength (MPa)	Maximum strain (%)	Density (kg/m^3)
1.99 ± 0.22	26.75 ± 4.00	2.53 ± 0.15	845 ± 6

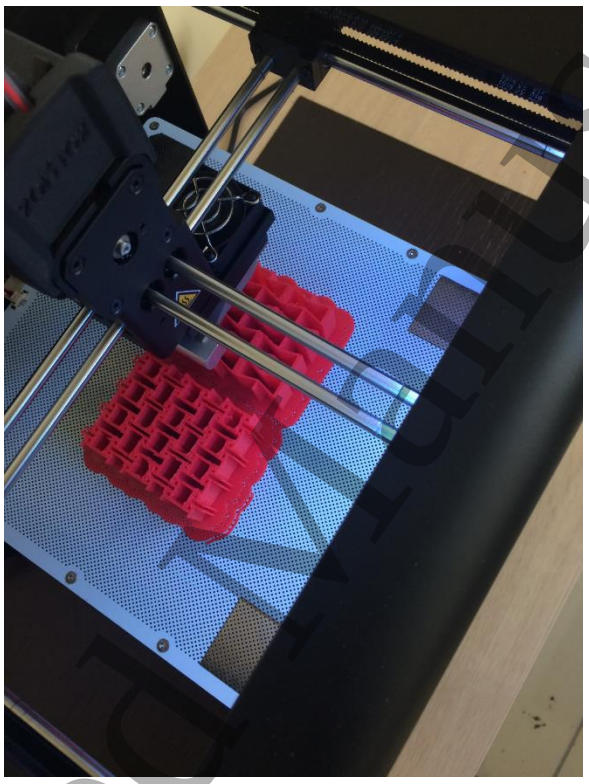

Figure 5. Production of anti-tetrachiral and re-entrant hexagonal samples.

4. NUMERICAL ANALYSES

Finite element analyses are conducted using the explicit solver of ABAQUS software. Quasi-static crushing state based on experimental conditions has been created using mass scaling method in the solver to decrease the computational costs. Kinetic energy should not overpass 10% of internal energy to obtain the correct result while using the mass scale [48]. Numerical models of manufactured lattices are represented in Figure 6 and 7. Regarding the complex shape, the automatic mesh was generated by taking

into the account of the maximum deviation factor as 0.1 and a minimum fraction of global size as 0.9. As a result, approximately 670000 solid C3D8R elements were created for 0.4 mm unit mesh input.

The models consist of the rigid top plate, the auxetic sample with solid elements and rigid plate at below. The top plate is free only in the axial direction. Force-displacement boundary condition has been applied to simulate experimental condition. The interaction was created as “all with self” definition. Tangential and normal friction coefficients were deployed with a value of 0.2. Load-displacement curves have been produced and compared with experimental findings.

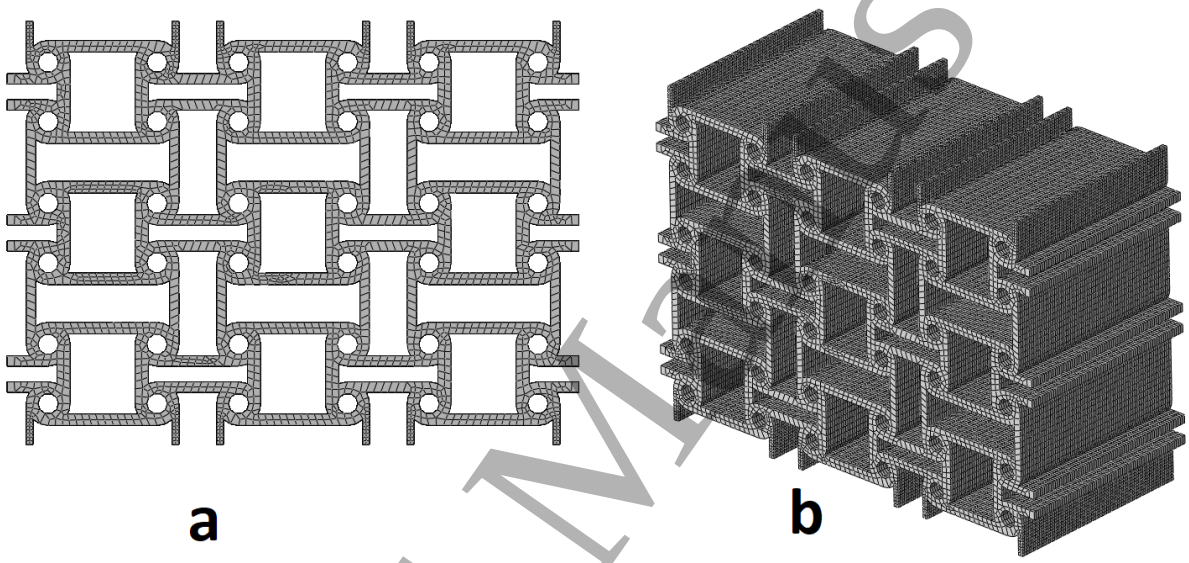

Figure 6. Anti-tetrachiral lattice system a) front-view b) perspective-view.

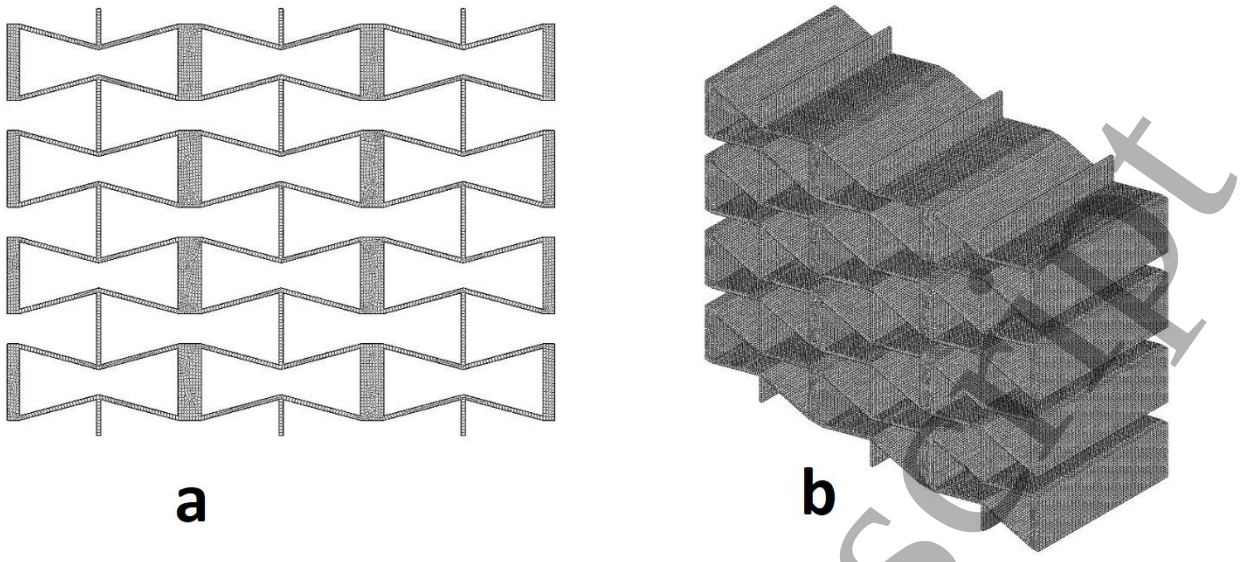

Figure 7. Re-entrant hexagonal lattice system a) front-view b) perspective-view.

5. RESULTS

5.1. Experimental Results

The load-deflection diagrams characterize the energy absorption capacity of crashworthy structures and can be divided into three phases which are elastic, plateau, and densification phases. Amongst them, a low amount of the energy can be absorbed by elastic deformation while the larger amount of deformation energy is absorbed by the plastic deformation and fracture. Thus, a longer plateau phase is desired for the better energy absorption of the crashworthy structures. The energy absorption (EA) is calculated from the area under the load-deflection curve as in Figure 10. The test curve which was drawn for 240 seconds showed a dramatic increase in the load due to the fact that the densification phase has started. Densification phase is not principally taken into the account for judgement of energy-absorbing capability of the manufactured samples. The calculation for the energy absorption is defined as

$$EA = \int_0^d F d\delta, \tag{7}$$

in which F is reaction force in the crushing process, and d denotes the maximum deflection until the densification phase. Therefore, the onset deflection of the densification phase is needed to be determined to define where the plateau phase ends, and the densification phase starts. In literature, there are several ways to define

the onset deflection of densification, such as intersecting the tangents of densification phase and load/stress plateau phase [49–51], picking a last local minimum deflection/strain point before dramatic increase [52,53], and specifying a point using the same tangent of elastic phase [51], however, an energy efficiency parameter, $\eta(\delta)$, expressed in Equation in 8,

$$\eta(\delta) = \frac{1}{F(\delta)} \int_0^d F(\delta) d\delta \tag{8}$$

is used in this study to determine the onset deflection of densification numerically and consistently [54,55]. By the means of the energy absorption efficiency, a representative onset deflection of densification is defined in which the energy absorption efficiency reaches the highest point on the efficiency-deflection plot, it is expressed in Equation 9,

$$\left. \frac{d\eta(\delta)}{d\delta} \right|_{\delta=d} = 0 \tag{9}$$

The energy absorption capability can be captured via specific energy absorption (SEA) as defined in Equation 10,

$$SEA = EA/m \tag{10}$$

which expresses the amount of dissipated energy divided by structural mass (m). Besides, mean crushing force (MCF) is another efficiency parameter to be considered to observe crashworthiness capacity of the structure which is given below.

$$MCF = \frac{1}{d} \int_0^d F d\delta \tag{11}$$

Regarding the occupant safety of a vehicle, mean crushing force is divided by peak crushing force (PCF), which is the highest force in the load-deflection curve, to obtain crushing force efficiency (CFE) that is aimed to be close to 1 [22] as defined in Equation 12,

$$CFE = \frac{MCF}{PCF} \quad (12)$$

Comparison of energy-deflection, force-deflection and mean crushing force-deflection curves are other efficiency measurement tools. The cellular structures exhibit normally three regimes in the force-deflection response. After the initial elastic region is completed, the plateau regime that is the main energy absorption period for the crushed structure starts and generally continues in the same level of force. Higher force level in the plateau regime makes the structure better energy absorber. A nominal stress-strain curve or mean crushing force-deflection curves are used to compare the crushing efficiency of different cellular structures. Their plateau regimes are observed to understand the energy absorption capacity in terms of mean crushing force- and/or stress. When the plastic collapse reaches the limit, the densification phase starts, and force increase to extremely a high level. The impact energy should be dissipated before the crushing has arrived at this section.

Crushing tests for both anti-tetrachiral and re-entrant hexagonal are illustrated in Figure 8 and 9, respectively. It seems that all tests for anti-tetrachiral and re-entrant lattices show a similar trend in their group. Figure 10 depicts a comparison of anti-tetrachiral and re-entrant curves. Anti-tetrachiral lattices absorb more energy thanks to their collapse mechanism that depends on ligaments bending and node rotation on the four corners of each lattice. Differently, from thin-walled metal tubular structures commonly used under axial crushing loading for crashworthiness purpose, MCF curves of current geometries exhibited increasing energy absorption response. That behavior is promising to use them as a candidate for filling of the thin-walled crash absorbers to increase crashworthiness ability. From the calculation of the onset deflection of densification via the energy efficiency parameter, the densification phase of anti-tetrachiral and re-entrant geometries started at 25.32 mm and 26.14 mm deflection, respectively.

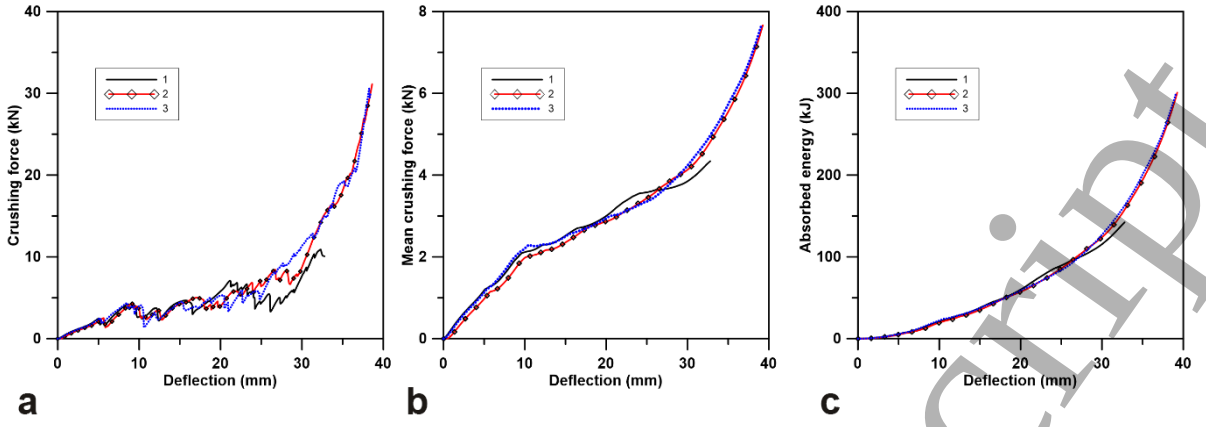

Figure 8. a) Force-deflection b) mean crushing force-deflection c) energy absorption-deflection curves of anti-tetrachiral lattices at 10 mm/min velocity.

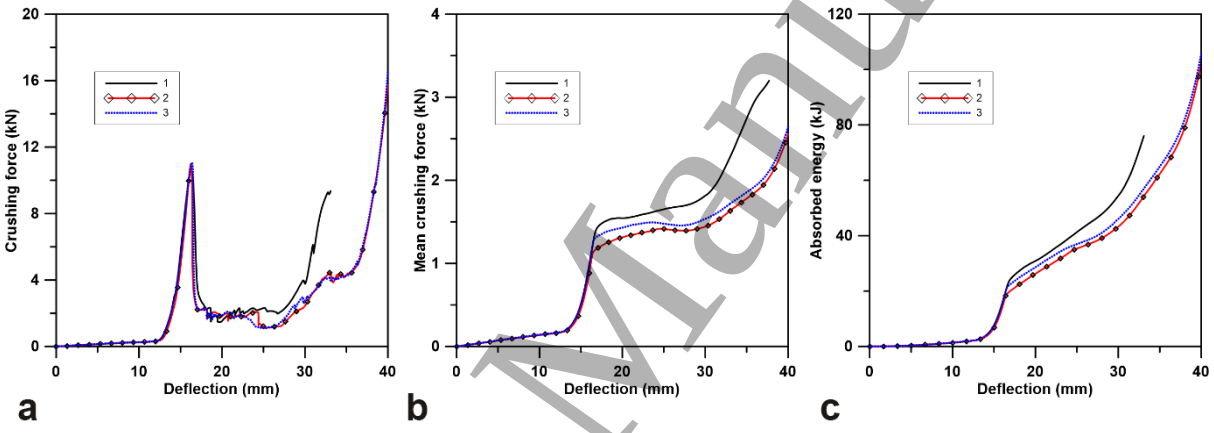

Figure 9. a) Force-deflection b) mean crushing force-deflection c) energy absorption-deflection curves of re-entrant hexagonal lattices at 10 mm/min velocity.

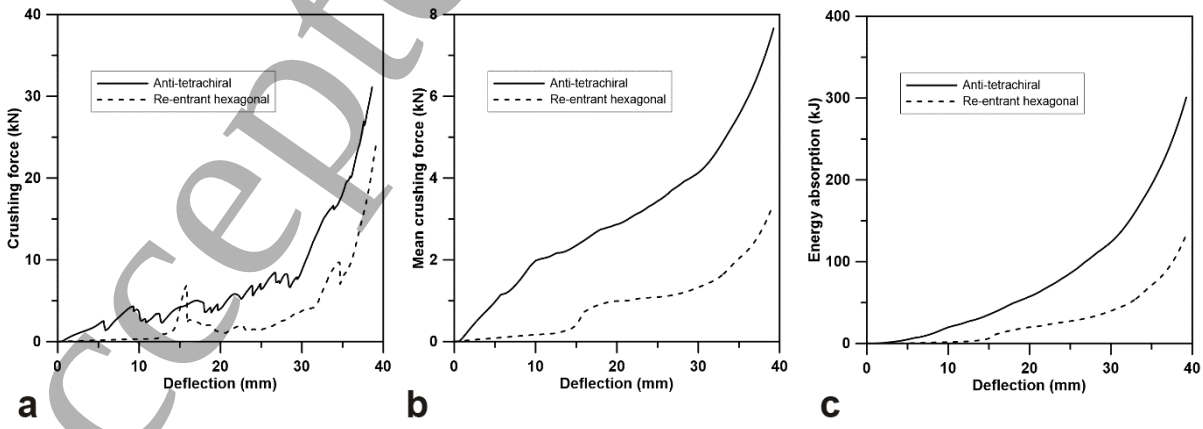

Figure 10. a) Force-deflection b) mean crushing force-deflection c) energy absorption-deflection curve comparison between anti-tetrachiral and re-entrant hexagonal structure at 10 mm/min velocity.

5.2. Deformation modes

After the elastic deformation phase completed, plastic collapses and local bucklings on the struts are observed for each design. The collapse occurs via bending around the ligament (edge circles) of the anti-tetrachiral lattices. However, the existence of these ligaments provides higher bending stiffness against the expected collapse. For instance, when the bending moment around the ligaments reached a high level, the vertical struts of the top lattices could not withstand the compressive load and failed after 5 mm deflection. Moreover, these broken struts contacting with the top surface were marked with arrows as in Figure 11. The auxetic behavior continues until around 7 mm deflection. Lower struts start to break and slightly slanting was become visible at around 10 mm deflection. Then, the contact between lattice walls and resistive effect of ligaments caused a high reaction force through local bucklings and local contact forces between unite lattice walls. It seems that upper and bottom lattice rows collapsed locally and made a slanting movement; two lattice rows in the middle have not started to collapse after 15 mm deflection yet. The system endured until a high level of loading, later the material could not stand anymore and failed at the lower and upper part. So global buckling, slanting, and local collapses were observed together. Similar motion sequences were observed in all three repeated tests.

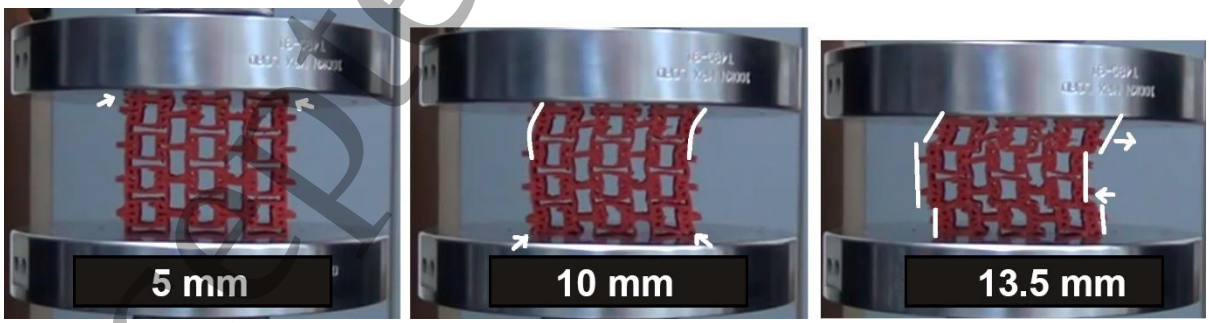

Figure 11. Critical crushing times of the anti-tetrachiral lattices.

Re-entrant hexagonal lattices show longer elastic phase, due to the nature of the unit cell. When the vertical struts and thick mid-walls of each array touch each other, the

structure starts to store the energy of elastic and plastic deformation due to the more constrained organization of unit cells. The collapse of this design shows that it collapses easier than anti-tetrachiral lattices. The struts between lattices in the original design are thickened to enhance energy absorption capability and not to separate of lattices from each other easily. λl represents the thickened sections in Figure 2. Figure 12 depicts a summary of the crushing characteristics of modified re-entrant hexagonal lattices. Both elastic and auxetic characteristics continue until almost 11.5 mm deflection. A significant number of local bucklings on the struts develop after 15 mm deflection. Subsequent phase shows an increase of local buckling events, however, after 17 mm deflection, slanting movement develops on the block of the lattices.

Figure 12. Critical crushing times of the modified re-entrant hexagonal lattices.

5.3. Comparison of experimental and numerical results

First, a mesh sensitivity study was conducted for different unit cell dimensions. The force-deflection comparison of numerical model and test is illustrated in Figure 13 and 14 for anti-tetrachiral and re-entrant lattices, respectively. Figure 15 depicts the correlation between the experimental and numerical results of the mean crushing force and absorbed energy, respectively. The crushing response of numerical models is matched well with the experimental results. However, experimental results of re-entrant hexagonal lattice system show more energy absorption compared to the numerical analysis. The imperfections, yield stress and stiffness of the material are the main parameters to predict the response of the design. Due to the nature of 3D FDM printing process of ABS polymer material, anisotropy, brittleness and imperfection cause some differences in predicting buckling deformation or buckling shape of the lattice systems. Although the behavior of the material is assumed as isotropic in numerical analyses, the results were close to that of the experiment.

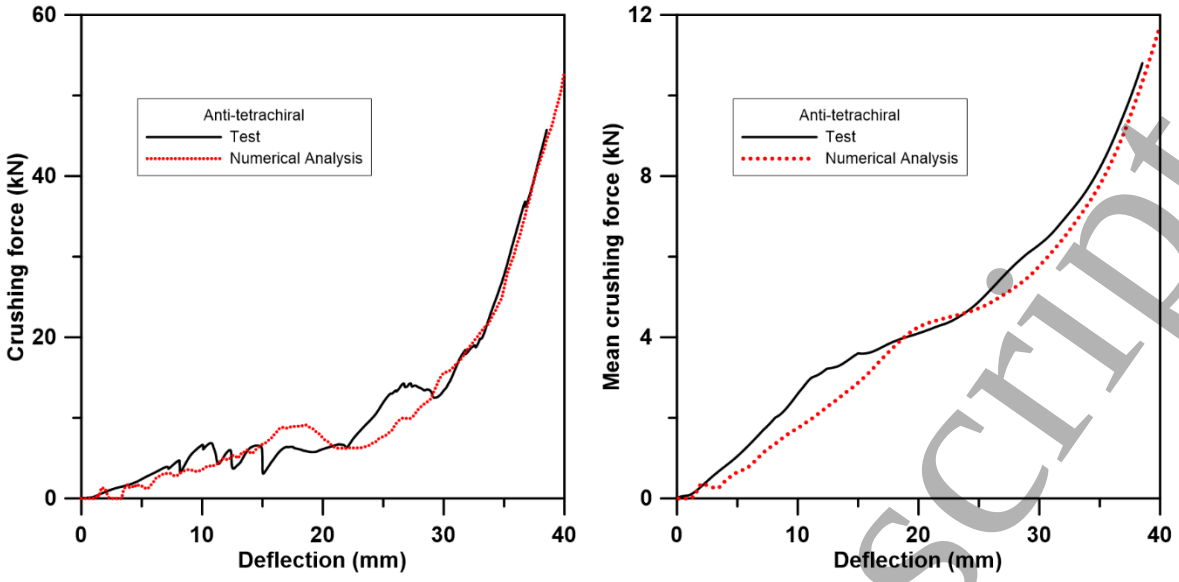

Figure 13. Comparison between numerical and experimental results of anti-tetrachiral lattices.

For better understanding, the elaboration of numerical results is needed. In the experimental results of the anti-tetrachiral lattices, it is shown that the vertical struts of the top lattices failed at 5 mm deflection in a local buckling and crushing manner and this phenomenon causes an almost linear increase of the crushing force as it is seen in Figure 15. Besides, slight slanting can be monitored on the left upper side of the anti-tetrachiral lattices which whipped up the sliding of the middle unit cell network and premature global buckling. However, in the FEM analysis, this phenomenon is not deployed to prevent the increase of computational cost due to the usage of failure criteria. Instead of buckling and crushing, upper and lower vertical struts touching the crushing plates slid out of the geometrical boundaries and become lateral in the range of 5 to 15 mm deflection. The global buckling is observed in the experiment under 10 mm deflection, however, in the analysis, it is not experienced even under high local buckling formation due to lack of failure. The onset of global buckling can be seen under the 15 mm deflection in the FEM analysis, where the same deformation pattern and crushing load is obtained under the 20 mm deflection in the experimental results. After the displacement of 30 mm, where the densification phase is strongly dominating, the correlation of FEM and experimental results are high by reason of crushed lattices behave like a constituent solid material in the densification phase.

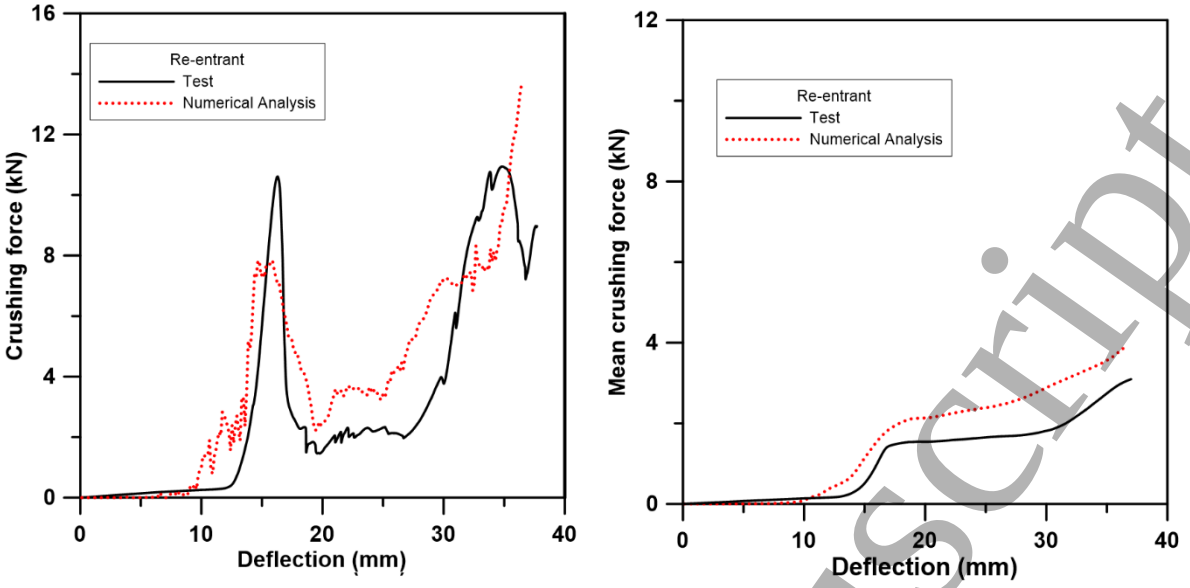

Figure 14. Comparison between numerical and experimental results of re-entrant lattices

Considering modified re-entrant lattices, in the experimental results, the local buckling of struts starts from the vertical struts on the lower-right side of the lattice structure. The local buckling of mentioned strut under 5 mm deflection triggers the failure of lower and upper vertical struts. However, in the analysis, local buckling formation starts from the upper vertical struts on both sides. Upper and lower vertical middle struts experienced only compression deformation without any local buckling until 15.5 mm deflection. Under the 10 mm deflection, deformations are observed in both the upper and lower side of the lattice structure but in the analysis, deformation starts only from the upper side and it proceeds to 15 mm stroke. In the modified re-entrant structures, vertical thick mid-wall elements are important to absorb energy by compression without performing any premature buckling. For this phenomenon, they start to touch each other after local collapses on the vertical axis to absorb more energy. In the analysis, this phenomenon is captured for the thick mid-walls but it cannot be captured for the vertical thinner struts on both sides. The dislocation of the thinner struts which are located on both sides of the modified re-entrant lattices can be explained by the lack of failure criteria in the analysis, and the local buckling behavior of the inner vertical thin struts forced to change the orientations of them. The densification phase results of experiment and FEM are quite far due to the higher inner gaps of anti-tetrachiral lattices.

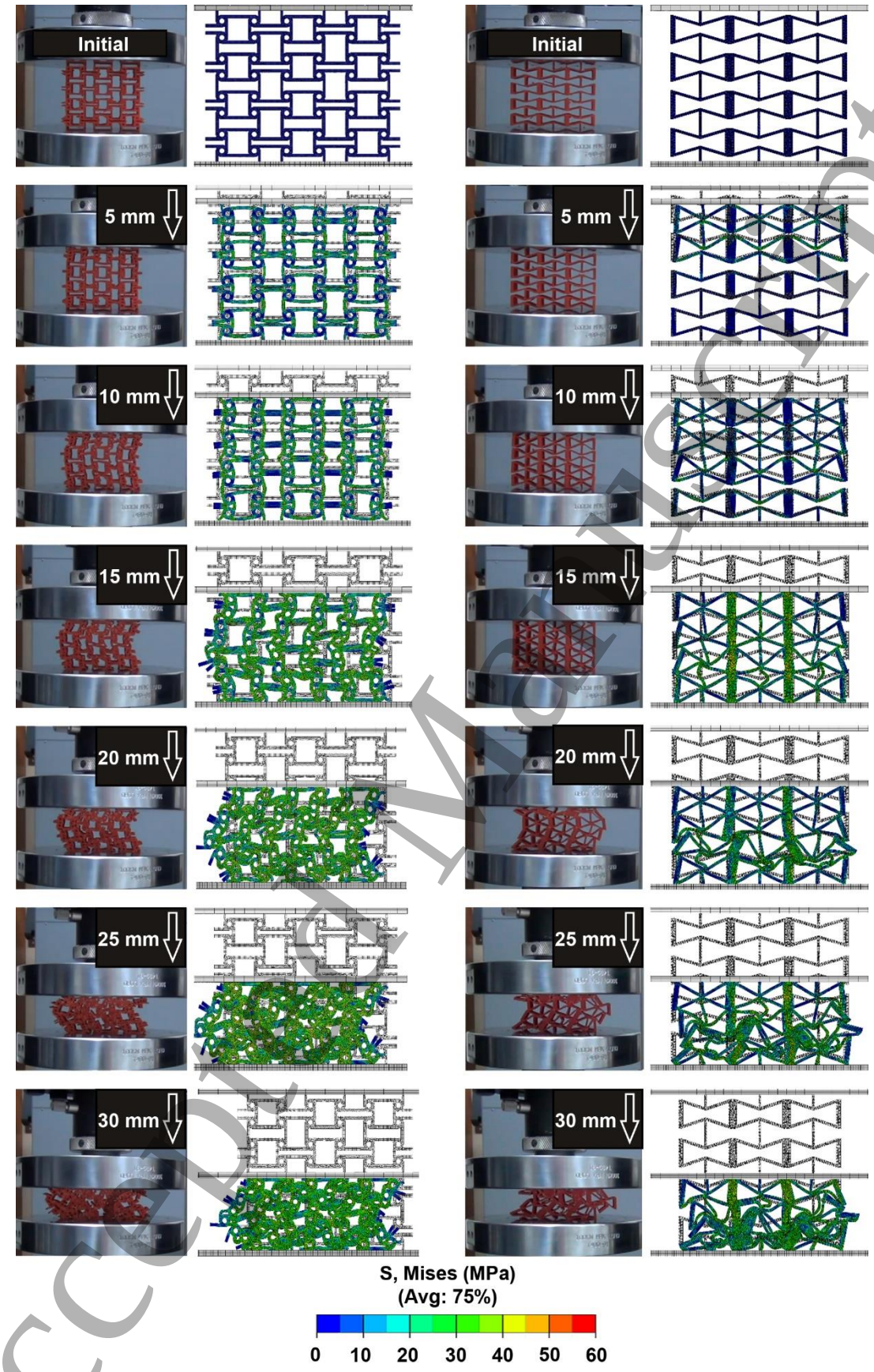

Figure 15. The deflection images of the samples at every 30 seconds from the initial to the final state at 180 seconds.

6. CONCLUSIONS

A comparison study on the in-plane quasi-static crushing response of anti-tetrachiral and modified re-entrant lattices have been presented. Anti-tetrachiral lattices showed better energy absorption capability than modified re-entrant lattices. Deformation modes exhibited similar results at repeated tests. Auxeticity was observed only in elastic deformation for both types. However, modified re-entrant lattices exhibited elastic deformation for a longer duration. Therefore, we can obtain lower reaction forces at modified re-entrant designs. The thick mid-walls are the source of the energy absorption mechanism of the re-entrant design.

Anti-tetrachiral lattices could only deform through two types of motions; slanting in several rows and local crushings in ligaments. That type of motion is closely related in-plane strength of lattices thanks to the corner ligaments. And repeated tests showed similar slanting motion. Theoretical prediction of the in-plane stiffness (E_y) through the value of vertical strut's ratio to ligament radius (α_y) was well-matched with the deformation modes of experiments. However, instability after increased deformation causes behavior which is difficult to predict due to material inhomogeneity, defects, and defects location. Therefore, further parametric and experimental investigation regarding instabilities can benefit the understanding of the theoretical estimation.

The numerical crushing study succeeded for both geometries and captured the results of tests well. The mass scale method is used to decrease computational costs. Basic modes were captured similar in both experiments and analyses. That gives the opportunity to model new anti-tetrachiral and modified re-entrant cells with new design purposes and without new manufacturing costs. However, it should be pointed out that several fractures observed in the tests require fracture characterization of the struts to observe or take into account possible other effects such as released energy.

REFERENCES

[1] H. Li, Y. Ma, W. Wen, W. Wu, H. Lei, D. Fang, In Plane Mechanical Properties of Tetrachiral and Antitetrachiral Hybrid Metastructures, J. Appl. Mech. 84 (2017) 081006. doi:10.1115/1.4036937.

[2] K.E. Evans, M.A. Nkansah, I.J. Hutchinson, S.C. Rogers, Molecular network design, Nature. 353 (1991) 124–124. doi:10.1038/353124a0.

[3] W. Wu, W. Hu, G. Qian, H. Liao, X. Xu, F. Berto, Mechanical design and multifunctional applications of chiral mechanical metamaterials: A review, Mater. Des. 180 (2019) 107950. doi:10.1016/J.MATDES.2019.107950.

[4] W. Wu, X. Song, J. Liang, R. Xia, G. Qian, D. Fang, Mechanical properties of anti-tetrachiral auxetic stents, Compos. Struct. 185 (2018) 381–392. doi:10.1016/J.COMPSTRUCT.2017.11.048.

[5] X.L. Ruan, J.J. Li, X.K. Song, H.J. Zhou, W.X. Yuan, W.W. Wu, R. Xia, Mechanical Design of Antichiral-Reentrant Hybrid Intravascular Stent, Int. J. Appl. Mech. 10 (2018) 1850105. doi:10.1142/S1758825118501053.

[6] W. Wu, L. Geng, Y. Niu, D. Qi, X. Cui, D. Fang, Compression twist deformation of novel tetrachiral architected cylindrical tube inspired by towel gourd tendrils, Extrem. Mech. Lett. 20 (2018) 104–111. doi:10.1016/J.EML.2018.02.001.

[7] C. Ma, H. Lei, J. Liang, W. Wu, T. Wang, D. Fang, Macroscopic mechanical response of chiral-type cylindrical metastructures under axial compression loading, Mater. Des. 158 (2018) 198–212. doi:10.1016/J.MATDES.2018.08.022.

[8] H. Yu, W. Wu, J. Zhang, J. Chen, H. Liao, D. Fang, Drastic tailorable thermal expansion chiral planar and cylindrical shell structures explored with finite element simulation, Compos. Struct. 210 (2019) 327–338. doi:10.1016/J.COMPSTRUCT.2018.11.043.

[9] R. Lakes, Foam Structures with a Negative Poisson's Ratio., Science. 235 (1987) 1038–40. doi:10.1126/science.235.4792.1038.

[10] A. Alderson, K.L. Alderson, D. Attard, K.E. Evans, R. Gatt, J.N. Grima, W. Miller, N. Ravirala, C.W. Smith, K. Zied, Elastic constants of 3-, 4- and 6-connected chiral and anti-chiral honeycombs subject to uniaxial in-plane loading, Compos. Sci. Technol. 70 (2010) 1042–1048. doi:10.1016/J.COMPSCITECH.2009.07.009.

[11] J. Dirrenberger, S. Forest, D. Jeulin, Effective elastic properties of auxetic microstructures: anisotropy and structural applications, Int. J. Mech. Mater. Des. 9 (2013) 21–33. doi:10.1007/s10999-012-9192-8.

[12] J.N. Grima, E. Chetcuti, E. Manicaro, D. Attard, M. Camilleri, R. Gatt, K.E. Evans, On the auxetic properties of generic rotating rigid triangles, Proc. R. Soc. A Math. Phys. Eng. Sci. 468 (2012) 810–830. doi:10.1098/rspa.2011.0273.

[13] Y.J. Chen, F. Scarpa, Y.J. Liu, J.S. Leng, Elasticity of anti-tetrachiral anisotropic lattices, Int. J. Solids Struct. 50 (2013) 996–1004.

doi:10.1016/J.IJSOLSTR.2012.12.004.

[14] W. Liu, N. Wang, J. Huang, H. Zhong, The effect of irregularity, residual convex units and stresses on the effective mechanical properties of 2D auxetic cellular structure, Mater. Sci. Eng. A. 609 (2014) 26–33. doi:10.1016/J.MSEA.2014.04.090.

[15] Y. Hou, R. Neville, F. Scarpa, C. Remillat, B. Gu, M. Ruzzene, Graded conventional-auxetic Kirigami sandwich structures: Flatwise compression and edgewise loading, Compos. Part B Eng. 59 (2014) 33–42. doi:10.1016/J.COMPOSITESB.2013.10.084.

[16] Y. Liu, H. Hu, A review on auxetic structures and polymeric materials, (2010). http://ira.lib.polyu.edu.hk/handle/10397/27029 (accessed July 5, 2019).

[17] M. Mir, M.N. Ali, J. Sami, U. Ansari, Review of Mechanics and Applications of Auxetic Structures, Adv. Mater. Sci. Eng. 2014 (2014) 1–17. doi:10.1155/2014/753496.

[18] W. Yang, Z.-M. Li, W. Shi, B.-H. Xie, M.-B. Yang, Review on auxetic materials, J. Mater. Sci. 39 (2004) 3269–3279. doi:10.1023/B:JMSC.0000026928.93231.e0.

[19] L.J. Gibson, M.F. Ashby, Cellular Solids, Cambridge University Press, Cambridge, 1997. doi:10.1017/CBO9781139878326.

[20] M.F. Ashby, L.J. Gibson, Cellular Solids Structure and Properties, Cambridge University Press, 1998.

[21] H. Nakamoto, T. Adachi, M. Higuchi, Approximate analysis of progressive deformation in honeycomb structures subjected to in-plane loading, Arch. Appl. Mech. 83 (2013) 379–396. doi:10.1007/s00419-012-0685-6.

[22] Z. Zhou, J. Zhou, H. Fan, Plastic analyses of thin-walled steel honeycombs with re-entrant deformation style, Mater. Sci. Eng. A. 688 (2017) 123–133. doi:10.1016/J.MSEA.2017.01.056.

[23] M. Assidi, J.-F. Ganghoffer, Composites with auxetic inclusions showing both an auxetic behavior and enhancement of their mechanical properties, Compos. Struct. 94 (2012) 2373–2382. doi:10.1016/J.COMPSTRUCT.2012.02.026.

[24] S. Gonella, M. Ruzzene, Homogenization and equivalent in-plane properties of two-dimensional periodic lattices, Int. J. Solids Struct. 45 (2008) 2897–2915. doi:10.1016/J.IJSOLSTR.2008.01.002.

[25] A. Bacigalupo, M.L. De Bellis, Auxetic anti-tetrachiral materials: Equivalent elastic properties and frequency band-gaps, Compos. Struct. 131 (2015) 530–544. doi:10.1016/J.COMPSTRUCT.2015.05.039.

[26] J. Huang, Q. Zhang, F. Scarpa, Y. Liu, J. Leng, In-plane elasticity of a novel auxetic honeycomb design, Compos. Part B Eng. 110 (2017) 72–82. doi:10.1016/J.COMPOSITESB.2016.11.011.

[27] A. Lorato, P. Innocenti, F. Scarpa, A. Alderson, K.L. Alderson, K.M. Zied, N. Ravirala, W. Miller, C.W. Smith, K.E. Evans, The transverse elastic properties of chiral honeycombs, Compos. Sci. Technol. 70 (2010) 1057–1063. doi:10.1016/J.COMPSCITECH.2009.07.008.

[28] C. Lira, F. Scarpa, Y.H. Tai, J.R. Yates, Transverse shear modulus of SILICOMB cellular structures, Compos. Sci. Technol. 71 (2011) 1236–1241. doi:10.1016/J.COMPSCITECH.2011.04.008.

[29] Y.J. Chen, F. Scarpa, Y.J. Liu, J.S. Leng, Elasticity of anti-tetrachiral anisotropic lattices, Int. J. Solids Struct. 50 (2013) 996–1004. doi:10.1016/J.IJSOLSTR.2012.12.004.

[30] W. Wu, Y. Tao, Y. Xia, J. Chen, H. Lei, L. Sun, D. Fang, Mechanical properties of hierarchical anti-tetrachiral metastructures, Extrem. Mech. Lett. 16 (2017) 18–32. doi:10.1016/J.EML.2017.08.004.

[31] L.L. Hu, Z.J. Wu, M.H. Fu, Mechanical behavior of anti-trichiral honeycombs under lateral crushing, Int. J. Mech. Sci. 140 (2018) 537–546. doi:10.1016/J.IJMECSCI.2018.03.039.

[32] L.L. Hu, Z.R. Luo, Z.Y. Zhang, M.K. Lian, L.S. Huang, Mechanical property of re-entrant anti-trichiral honeycombs under large deformation, Compos. Part B Eng. 163 (2019) 107–120. doi:10.1016/J.COMPOSITESB.2018.11.010.

[33] R. Xia, X. Song, L. Sun, W. Wu, C. Li, T. Cheng, G. Qian, Mechanical Properties of 3D Isotropic Anti-Tetrachiral Metastructure, Phys. Status Solidi. 255 (2018) 1700343. doi:10.1002/pssb.201700343.

[34] W. Wu, D. Qi, H. Liao, G. Qian, L. Geng, Y. Niu, J. Liang, Deformation mechanism of innovative 3D chiral metamaterials, Sci. Rep. 8 (2018) 12575. doi:10.1038/s41598-018-30737-7.

[35] Y. Chen, M.-H. Fu, A novel three-dimensional auxetic lattice meta-material with enhanced stiffness, Smart Mater. Struct. 26 (2017) 105029. doi:10.1088/1361-665X/aa819e.

[36] X. Zhang, H. Ding, L. An, X. Wang, Numerical Investigation on Dynamic Crushing Behavior of Auxetic Honeycombs with Various Cell-Wall Angles, Adv. Mech. Eng. 7 (2015) 679678. doi:10.1155/2014/679678.

[37] A. Ingrole, A. Hao, R. Liang, Design and modeling of auxetic and hybrid honeycomb structures for in-plane property enhancement, Mater. Des. 117 (2017) 72–83. doi:10.1016/J.MATDES.2016.12.067.

[38] X. Ren, J. Shen, P. Tran, T.D. Ngo, Y.M. Xie, Design and characterisation of a tuneable 3D buckling-induced auxetic metamaterial, Mater. Des. 139 (2018) 336–342. doi:10.1016/J.MATDES.2017.11.025.

[39] Z. Dong, Y. Li, T. Zhao, W. Wu, D. Xiao, J. Liang, Experimental and numerical studies on the compressive mechanical properties of the metallic auxetic reentrant honeycomb, Mater. Des. 182 (2019) 108036. doi:10.1016/J.MATDES.2019.108036.

[40] D. Xiao, Z. Dong, Y. Li, W. Wu, D. Fang, Compression behavior of the graded metallic auxetic reentrant honeycomb: Experiment and finite element analysis, Mater. Sci. Eng. A. 758 (2019) 163–171. doi:10.1016/J.MSEA.2019.04.116.

[41] D. Xiao, X. Kang, Y. Li, W. Wu, J. Lu, G. Zhao, D. Fang, Insight into the negative Poisson's ratio effect of metallic auxetic reentrant honeycomb under dynamic compression, Mater. Sci. Eng. A. 763 (2019) 138151.

doi:10.1016/J.MSEA.2019.138151.

[42] A. Lorato, P. Innocenti, F. Scarpa, A. Alderson, K.L. Alderson, K.M. Zied, N. Ravirala, W. Miller, C.W. Smith, K.E. Evans, The transverse elastic properties of chiral honeycombs, Compos. Sci. Technol. 70 (2010) 1057–1063. doi:10.1016/j.compscitech.2009.07.008.

[43] A.G. Evans, M.Y. He, V.S. Deshpande, J.W. Hutchinson, A.J. Jacobsen, W.B. Carter, Concepts for enhanced energy absorption using hollow micro-lattices, Int. J. Impact Eng. 37 (2010) 947–959. doi:10.1016/J.IJIMPENG.2010.03.007.

[44] A. Ajdari, H. Nayeb-Hashemi, A. Vaziri, Dynamic crushing and energy absorption of regular, irregular and functionally graded cellular structures, Int. J. Solids Struct. 48 (2011) 506–516. doi:10.1016/J.IJSOLSTR.2010.10.018.

[45] J. Huang, Q. Zhang, F. Scarpa, Y. Liu, J. Leng, In-plane elasticity of a novel auxetic honeycomb design, Compos. Part B Eng. 110 (2017) 72–82. doi:10.1016/j.compositesb.2016.11.011.

[46] K. Günaydın, Z. Eren, H.S. Türkmen, Z. Kazancı, F. Scarpa, Axial low velocity impact response of anisotropic anti-tetrachiral filling lattices, in: 7th Int. Conf. Mech. Mater. Des., 2017: pp. 1053–1060.

[47] Zortrax, Material Data Sheet: Z-ABS, (2014).

[48] Abaqus Manual, 6.13.

[49] T.G. Nieh, K. Higashi, J. Wadsworth, Effect of cell morphology on the compressive properties of open-cell aluminum foams, Mater. Sci. Eng. A. 283 (2000) 105–110. doi:10.1016/S0921-5093(00)00623-7.

[50] A. Paul, U. Ramamurty, Strain rate sensitivity of a closed-cell aluminum foam, Mater. Sci. Eng. A. 281 (2000) 1–7. doi:10.1016/S0921-5093(99)00750-9.

[51] K.C. Chan, L.S. Xie, Dependency of densification properties on cell topology of metal foams, Scr. Mater. 48 (2003) 1147–1152. doi:10.1016/S1359-6462(02)00593-6.

[52] M. Vural, G. Ravichandran, Microstructural aspects and modeling of failure in naturally occurring porous composites, Mech. Mater. 35 (2003) 523–536. doi:10.1016/S0167-6636(02)00268-5.

[53] K. Gunaydin, Z. Eren, F. Scarpa, Experimental investigation of auxetic structures subjected to quasi static axial load, in: 2017 8th Int. Conf. Recent Adv. Sp. Technol., IEEE, 2017: pp. 7–10. doi:10.1109/RAST.2017.8002986.

[54] X. Zhang, H. Ding, L. An, X. Wang, Numerical Investigation on Dynamic Crushing Behavior of Auxetic Honeycombs with Various Cell-Wall Angles, Adv. Mech. Eng. 7 (2015) 679678. doi:10.1155/2014/679678.

[55] Q.M. Li, I. Magkiriadis, J.J. Harrigan, Compressive Strain at the Onset of Densification of Cellular Solids, J. Cell. Plast. 42 (2006) 371–392. doi:10.1177/0021955X06063519.